



UPPSALA
UNIVERSITET

Studies of Gas-flow Metrology and Ion-beam Induced Desorption

Licentiate Thesis

2006

EMMA HEDLUND



Abstract

In this thesis aspects of vacuum metrology and vacuum science have been investigated. For vacuum metrology purposes, a throughput system is often used in order to calibrate vacuum gauges. An important component in such systems is the flowmeter, which has to deliver a pure and well-determined gas flow into the system. The gas flow is determined by measuring the pressure inside the flowmeter. It has turned out though that the main contribution to the total uncertainty for the generated gas flow is the uncertainty of the pressure measurements. An alternative way to determine the gas flow generated from the flowmeter would be to use laser refractometry to monitor dynamic gas density *in situ* in the flowmeter. In this thesis a feasibility study of how laser refractometry could improve the calibration of vacuum gauges is reported.

A problem in vacuum science is the observed large pressure rises, up to several orders of magnitude, during operation of the heavy-ion accelerators at GSI, CERN and BNL. The pressure rise is believed to be due to ion-beam loss induced desorption. It is of interest to investigate how the desorption yield η (released molecules per incident ion) scales with the electronic energy loss dE/dx . First experiments were made with U^{73+} beam impacting on 316LN and P506 stainless steel, OFE copper and aluminum targets for the energies 15, 40, 100, 408 and 1000 MeV/u. In a second experiment an Ar^{10+} beam was impacting on 316LN stainless steel for 40, 80 and 100 MeV/u. The measured effective desorption yields have been compared with different theoretical models for sputtering, predicting an exponential scaling of the energy loss with exponents between 2 and 3.

Contents

| | |
|---|----|
| 1. Introduction..... | 1 |
| 2. Laser refractometry..... | 3 |
| 2.1 Interferometers..... | 3 |
| 2.2 Free spectral range..... | 4 |
| 2.3 The planned setup..... | 5 |
| 3. Ion-beam induced desorption..... | 7 |
| 3.1 The SIS18 synchrotron..... | 7 |
| 3.2 The test-stand..... | 8 |
| 4. Summary of papers..... | 11 |
| 4.1 Paper I: Laser refractometry..... | 11 |
| 4.1.1 Gas flow as a function of refractive index..... | 11 |
| 4.1.2 Comparison of accuracies..... | 11 |
| 4.2 Paper II: Ion-beam induced desorption..... | 12 |
| 4.2.1 Energy dependence..... | 13 |
| 4.2.2 Ion dependence..... | 13 |
| 4.2.3 Target dependence..... | 14 |
| 4.2.4 Theoretical models..... | 14 |
| 5. Outlook..... | 17 |
| 6. Acknowledgements..... | 19 |
| 7 References..... | 21 |

1. Introduction

When most people think about vacuum, they consider it to be a space containing nothing. In reality vacuum is defined as a volume with subatmospheric pressure, and such thing as an ideal vacuum containing nothing is not possible to achieve. There are different classifications of vacuum starting from “low vacuum” down to “extreme high vacuum”, see Table 1.

Table 1: Classification of vacuum

| | |
|---------------------------|-------------------------|
| Low vacuum | $10^2 - 10^5$ Pa |
| Medium vacuum | $10^{-1} - 10^2$ Pa |
| High vacuum (HV) | $10^{-6} - 10^{-1}$ Pa |
| Ultra high vacuum (UHV) | $10^{-10} - 10^{-6}$ Pa |
| Extreme high vacuum (XHV) | $< 10^{-10}$ Pa |

The highest vacuum achieved today in a laboratory is $5 \cdot 10^{-12}$ Pa [1]. The best vacuum, however, is the natural vacuum in the outer space, where a typical pressure is in the 10^{-17} Pa region, which corresponds to 0.25 particles per cubic meter [2]. The vacuum of space is mostly filled with plasma, but there are also large numbers of photons.

The first common use of vacuum was in light bulbs to protect the tungsten filament from burning out to quickly. Today, high vacuum and ultra high vacuum are used in a wide variety of applications such as thin film coating, surface engineering, accelerator based science, semiconductor fabrication, freeze drying and pharmaceuticals.

In both industrial processes and research experiments it is of importance to know that you make correct measurements. Therefore vacuum metrology in e.g. form of calibration of vacuum gauges are important. One of the most used systems for calibration of vacuum gauges is the throughput system, see Figure 1:

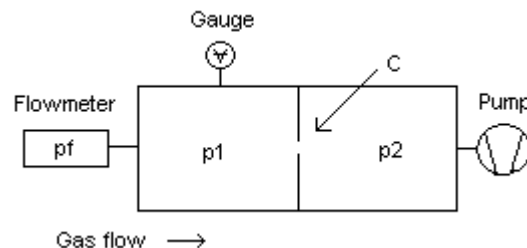


Figure 1: The throughput system. By knowing the gas flow generated from the flowmeter and the conductance of the small orifice, the pressure P_1 can be calculated.

By knowing the gas flow generated from the flowmeter and the conductance of the small orifice, the pressure P_1 can be calculated [3]. It has turned out though, that a large contribution to the accuracy of the throughput system comes from the flowmeter.

The largest problems in creating a good and stable vacuum are connected with outgassing. Outgassing is when gas is released from materials in a vacuum system. This can happen in several ways [4]:

Diffusion is the transport of one material through another one. The gas can diffuse either from the bulk to the surface or by permeation from the outside.

Outgassing is the net effect of diffusion plus desorption from the surface, and readsorption on the surface.

Thermal desorption is the release of gases caused by heating of the vacuum system. The gases released are the ones that were previously adsorbed on the interior wall of the system or on the chamber surface.

Dynamic outgassing, or ion induced desorption, is where outgassing is stimulated, for instance by part of an ion beam in a particle accelerator hitting the vacuum chamber wall, causing gas to be released.

2. Laser refractometry

Laser refractometry is a technique that measures how the speed of light is changed by the gas density of the substance, which is directly proportional to the refractive index of the substance. It is a very precise technique; the resolution of the laser refractometry measurements of gas density has been shown to be in the order of parts in 10^5 [5]. We are therefore interested to investigate whether laser refractometry can be employed instead of vacuum gauges and thereby obtain measurements of gas flow with higher accuracy.

2.1 Interferometers

The working principle is splitting an optical wave and then allowing the waves back together. If the two waves brought together coincide with the same phase they will amplify each other – interfere constructively - while if the two waves have opposite phases they will cancel each other out. The basic building blocks are a monochromatic source (e.g. laser), mirrors and a detector. Two common types of refractometer are the Michelson interferometer and the Fabry-Perot interferometer [6]. In the Michelson interferometer a semitransparent mirror (so called beam splitter) divides the wave into two, where one wave will hit a fixed mirror and the other will hit a movable mirror, see Figure 2. When the beams are brought back together, an interference pattern results.

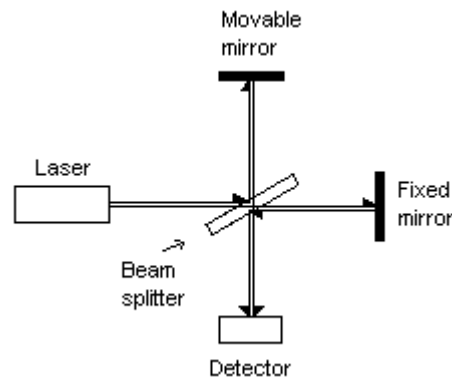


Figure 2: *The Michelson interferometer*

A Fabry-Perot interferometer is made of two parallel highly-reflecting mirrors, see Figure 3. A beam goes through the first mirror, and then, because of the high reflectivity of the mirrors, the beam will bounce between the mirrors many times. However, each time the light reaches the surface of the second mirror part of the light will be transmitted. This results in several beams that can interfere with each other. Due to the large number of interfering rays, the Fabry-Perot interferometer has extremely high resolution.

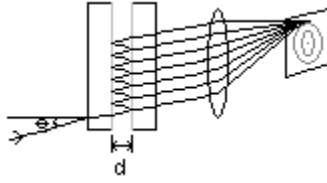


Figure 3: *The Fabry-Perot interferometer*

Because of the high resolution, simplicity and compactness of the setup, the Fabry-Perot interferometer has been chosen for this feasibility study.

2.2 Free spectral range

In a Fabry-Perot interferometer the distance d between the mirror plates affects the distance between the transmission peaks: the shorter the distance between the mirrors the larger the difference will be between the peaks, the so called free spectral range (FSR), according to

$$FSR = \frac{c}{2d} \quad (1)$$

The value of the width at half maximum of the transmission peak, $\Delta\nu/2$, will scale with the value of the free spectral range as

$$\frac{\Delta\nu}{2} = \frac{FSR}{2 \cdot F} \quad (2)$$

where F is the finesse. The finesse is commonly approximated (for reflectivity $R > 0.5$) by:

$$F = \frac{\pi\sqrt{R}}{1 - R} \quad (3)$$

Since our setup only allows us to have a rather short distance between the mirrors, approximately $d = 1$ mm, we will have large difference between the peaks. One way to compensate for the bad FSR is to make sure to get as good finesse factor as possible. As can be seen from Figure 4, mirrors with high finesse will give sharper transmission peaks and lower transmission minima than mirrors with low finesse:

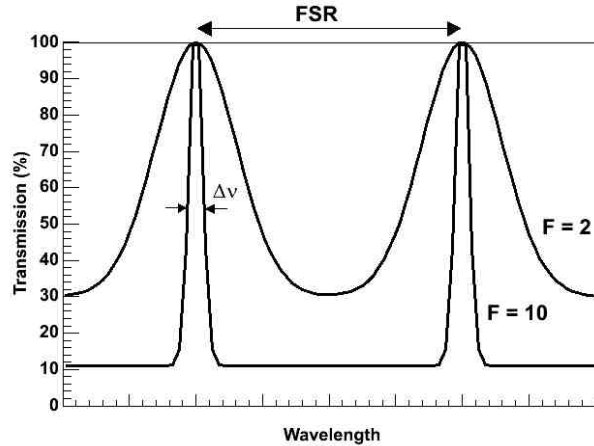


Figure 4: The transmission of a mirror as a function of wavelength. A mirror with high finesse has sharper transmission peaks and lower transmission minima than a mirror with low finesse.

To obtain as high finesse as possible you have to choose mirrors with as high reflectivity as possible. As can be seen from Figure 5, the finesse increases rapidly for mirrors with reflectivity higher than 0.95.

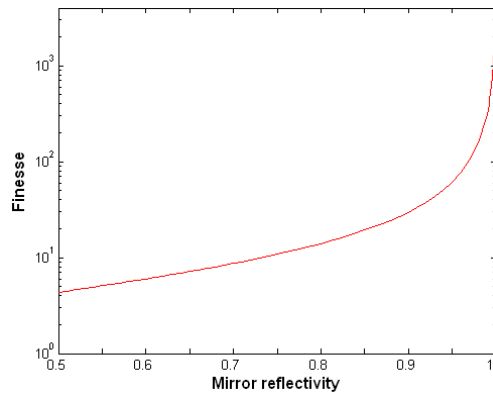


Figure 5: Finesse as a function of reflectivity. Very high finesse factors require highly reflective mirrors.

In our setup we have found mirrors with a reflectivity of $R = 99.999\%$ for a wavelength of 1064 nm.

2.3 The planned setup

Our planned setup, shown in Figure 6 [7] is based on heterodyne spectroscopy. This method is chosen since there will be enough accuracy to determine a frequency

difference of 10 kHz. A laser beam, with a wavelength of 1064 nm, passes through an isolator before entering the Fabry-Perot cell. After the cell, the beam is detected in a fast photo diode (bandwidth > 1 GHz). The current from the diode is led via an amplifier back to the current driver. This way it is possible to adjust the laser to the wanted peaks.

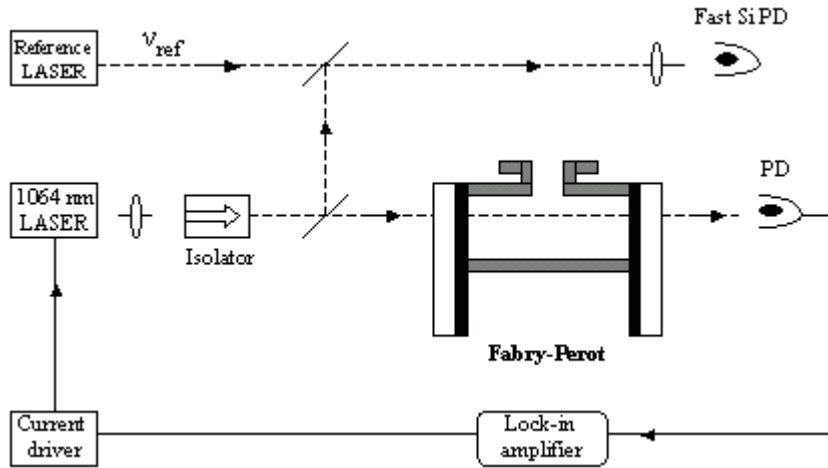


Figure 6: The planned setup is based on heterodyne spectroscopy in order to obtain enough accuracy to determine a frequency difference of 10 kHz [7].

3. Ion-beam induced desorption

During operation of heavy ion accelerators, some of the ions from the beam will be lost from the trajectory and finally hit the wall of the beam pipe [8]. When the wall is hit by a heavy ion, atoms or molecules are released from the surface. The desorbed molecules will in turn interfere with the beam and thereby decrease the quality and the intensity of the beam. It is therefore important to get more knowledge of the desorption process in order to minimize its influence on the beam.

3.1 The SIS18 synchrotron

The measurements presented in this thesis have been carried out at a beam line connected to the SIS18 synchrotron at GSI, Darmstadt, Germany. The SIS18 synchrotron has a circumference of 216 m and operates at 10^{-8} Pa, see Figure 7 [9]. Possible particle energies are in the range 50 – 2000 MeV/u depending on the specific heavy ions used.

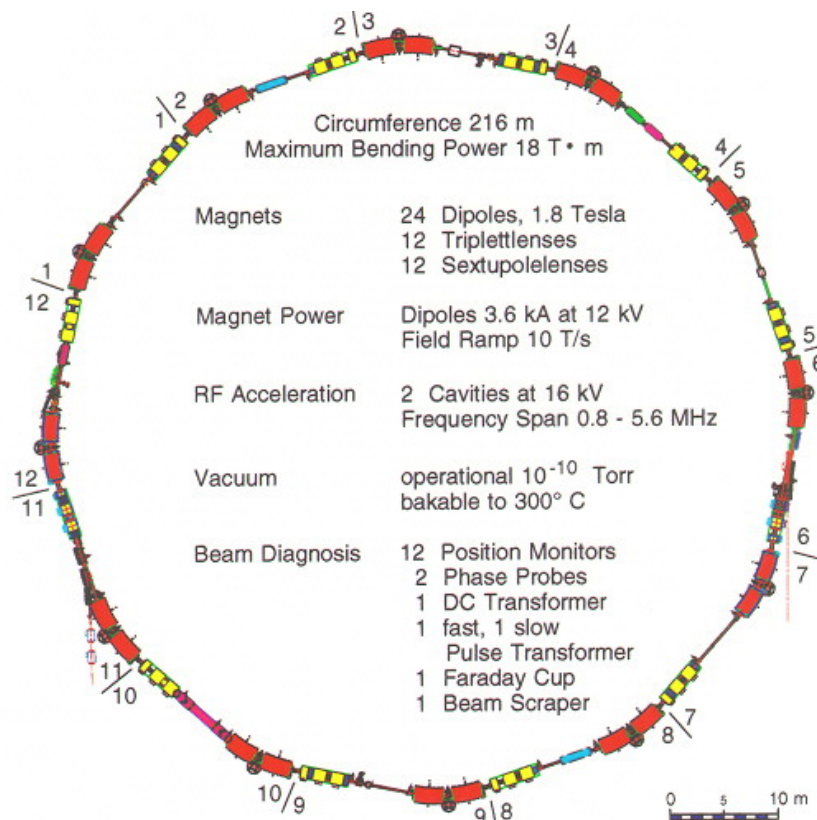


Figure 7: The SIS18 synchrotron has a circumference of 216 m [9].

The different possible beams and currents can be seen in Figure 8 [10]. We have used Ar and U beams with the following respective average beam currents: $1.5 \cdot 10^{10}$ particles/hit every 2 s for the argon beam and $2.4 \cdot 10^8$ particles per hit every 3.9 s for the uranium beam.

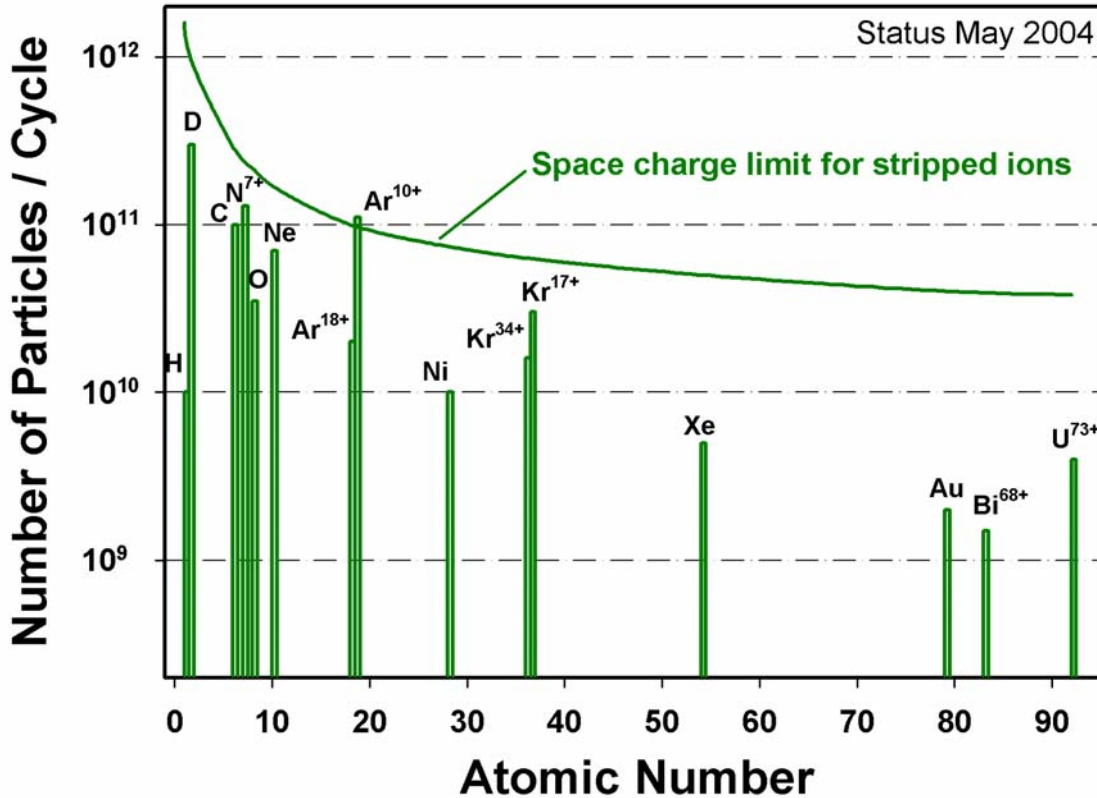


Figure 8: The different beam currents possible in SIS18 [10].

3.2 The test-stand

The experimental setup is shown in Figure 9 [11]. The beam coming from the left passes three different pumping stages before it will hit the target. The different pumping stages are needed in order to reduce the pressure from 10^{-5} Pa in the beam line to the required 10^{-9} Pa. The targets are 316LN stainless steel, P506 stainless steel, OFE copper and 6082 aluminum, all mounted on the rotational and movable feedthrough seen to the right in Figure 9. The thickness of the targets are chosen to be between 2 and 20 mm, which is thick enough to stop the beam.

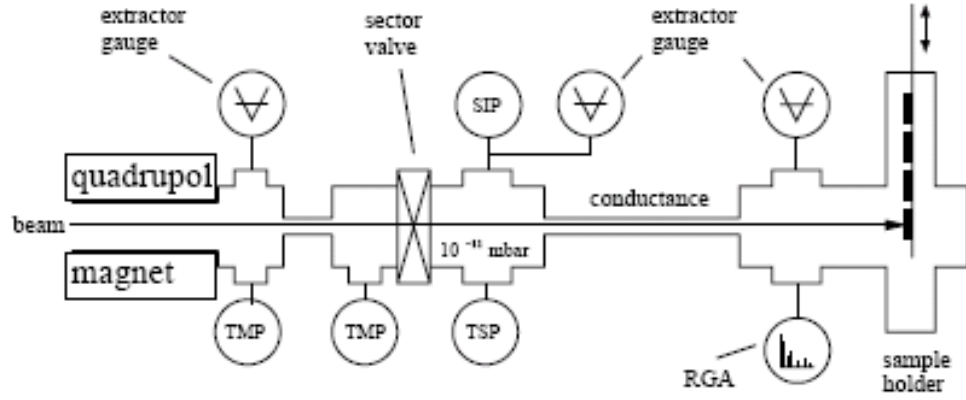


Figure 9: *The experimental setup [11].*

The effective desorption yield η_{eff} was calculated from the total pressure increase Δp using the ideal gas law,

$$\eta_{\text{eff}} = \frac{\Delta p \cdot S}{\dot{N} \cdot k_B \cdot T} \quad (4)$$

where S is the pumping speed, \dot{N} is the projectile ion flux, k_B the Boltzmann constant and T the temperature.

4. Summary of papers

4.1 Paper I: Laser refractometry

In this paper the relationship between gas flow and refractive index is shown. Then the accuracy of the laser refractometry method is investigated and compared with the accuracy of vacuum gauges.

4.1.1 Gas flow as a function of refractive index

The generated gas flow from the flowmeter has been determined from the ideal gas law and the Lorentz-Lorenz formula as the following relation:

$$q = RT \cdot \frac{\sum_i x_i}{\sum_i x_i A_i} \cdot \frac{2n}{3\nu} \cdot \frac{\Delta\nu}{\Delta t} \quad (5)$$

where R is the gas constant, T is temperature, n is refractive index, ν is the frequency of the laser, $\Delta\nu$ the change in frequency and Δt the time during the change in frequency.

4.1.2 Comparison of accuracies

The resolution of the laser refractometry method for measuring gas density is dependent of the pressure in the flowmeter but also on the distance between the mirrors. When the pressure decreases, the resolution will get worse by the same factor. By increasing the distance between the mirrors the resolution will improve by the same factor. The relative resolution of the gas density measurement for nitrogen is plotted as a function of the generated gas flow from the flowmeter, see Figure 10. For a comparison, the inaccuracy of the fill pressure measurement for nitrogen obtained with vacuum gauges, taken from the article by K. Jousten et al [3], is shown in the same plot.

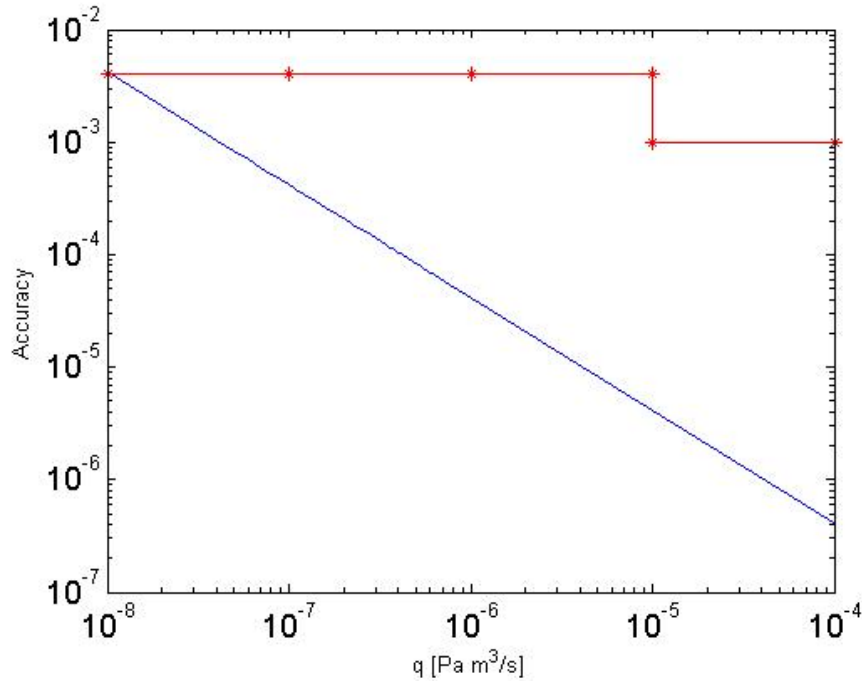


Figure 10: A plot of the inaccuracy as a function of the generated flow from the flowmeter. The solid line is the theoretical values of the resolution obtained by the laser refractometry method, and the line with stars is the inaccuracy coming from the fill pressure measurements by K. Jousten et al [3].

It can be seen from the plot that for the laser refractometry method the resolution is around $4 \cdot 10^{-7}$ for a gas flow of $1 \cdot 10^{-4}$ Pa m³/s, while the inaccuracy for the fill pressure measurement is $1 \cdot 10^{-3}$ for the same gas flow. The accuracy for the laser refractometry method is here roughly 3 orders of magnitude lower compared with the fill pressure measurements. But since the refractometry method is pressure dependent, the accuracy will increase linearly with lower pressure, and at a gas flow of $1 \cdot 10^{-8}$ Pa m³/s the accuracy of the both methods are the same. It is important to remember that our values are theoretical values, and those from [3] are experimental ones. For the laser refractometry method one should also take into account that a change in temperature will affect the refractive index of the gas as well as the measurement of the distance between the mirrors. However, the laser refractometry method is a promising new method for accurate measurements of the gas flow.

4.2 Paper II: Ion-beam induced desorption

We have investigated how the desorption yields from ion induced desorption depend on the energy of the incident ion, the type of incident ion and the target. The results are compared with theoretical models of sputtering, since no model for ion-beam induced desorption is available.

4.2.1 Energy dependence

The projectile energies were chosen to 15, 40, 100, 408 and 1000 MeV/u for the U^{73+} beam and 40, 80 and 100 MeV/u for the Ar^{10+} beam. The effective desorption yields for the respective beams on 316LN stainless steel are plotted in Figure 11. For the U^{73+} beam at 408 and 1000 MeV/u only upper limits of 200 particles per incident ion could be derived. These data points are therefore not included in the figure. One can clearly see that the effective desorption yield is decreasing with increasing projectile energy. An explanation to the decreasing energy dependence is discussed in section 4.2.4.

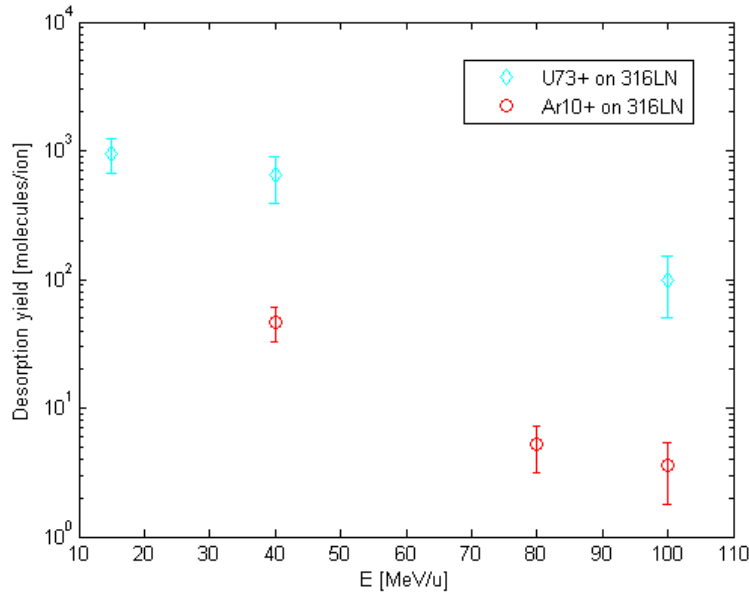


Figure 11: The obtained desorption yields from U^{73+} and Ar^{10+} beams impacting on 316LN stainless steel in the 15-100 MeV/u energy range

4.2.2 Ion dependence

The obtained desorption yield from the uranium beam is much higher than the desorption yield from the argon beam, see Figure 11. Except for the different masses, maybe also the different charge states could affect the desorption yield. From previous measurements at lower energies (< 1 MeV/u) the charge state has turned out to affect the desorption yield [12]. For higher projectile energies though, the equilibrium charge state distribution will be reached at a certain depth. From our data we cannot draw any conclusion on whether this depth is within the critical volume for desorption.

4.2.3 Target dependence

For the uranium beam we observe different desorption yields for the four different targets, see Figure 12. The general trend is that the yield from the copper target is lower than that of the other targets.

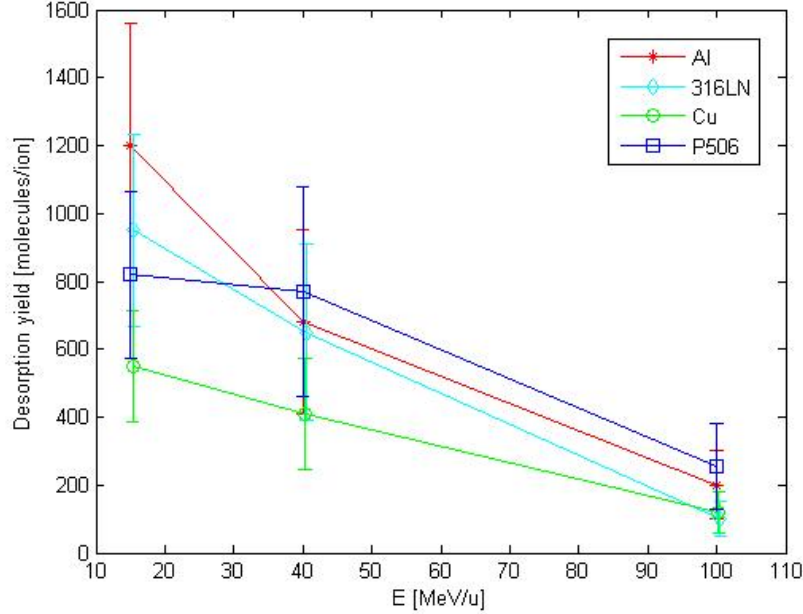


Figure 12: Desorption yields from uranium beam impacting on different targets.

4.2.4 Theoretical models

We are interested to investigate how the effective desorption yield, η_{eff} , scales with the energy loss, i.e. we would like to find the values for the exponent n from the following equation

$$\eta_{\text{eff}} = K \cdot \left(\frac{dE}{dx} \right)^n \quad (6)$$

The energy loss for uranium and argon can be obtained from the SRIM code [13]. It turns out that dE/dx for uranium is much higher than for argon for the same critical length in the sample. This could in part explain the higher desorption yields for uranium, see section 4.2.2. To obtain the exponent n , the measured desorption yield is plotted versus the corresponding energy loss obtained from the SRIM code, see Figure 13. The slope of the line gives the value of n . For the U^{73+} beam $n = 2.6 \pm 0.5$ and for the Ar^{10+} beam $n = 3.6 \pm 2.5$.

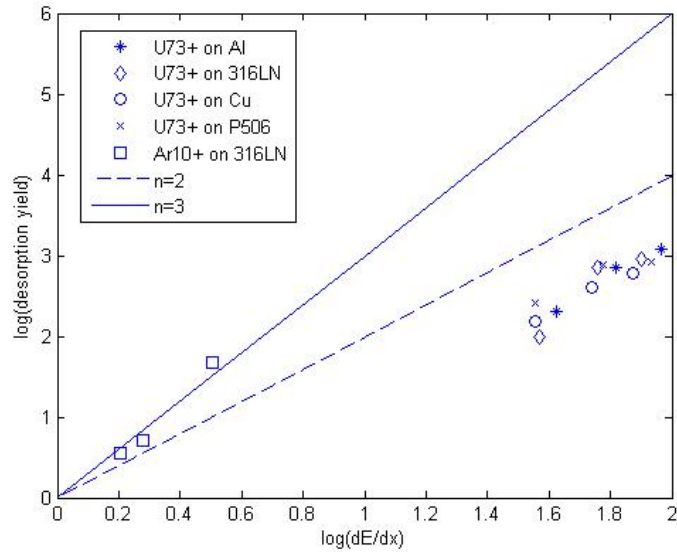


Figure 13: Effective desorption yields from aluminium, copper and stainless steel as a function of the energy loss. For Ar on 316LN $n = 3.6$. For the U beam on Cu we get $n = 1.9$, on 316LN $n = 2.9$ and on Al $n = 2.3$.

There are two theoretical models for sputtering covering the region $n=2$ to $n = 3$, namely the thermal spike model with $n = 2$ and the pressure pulse model with $n = 3$ [14, 15]. However, from our data it is not possible to fit them to a specific model. It is only possible to show the trend of the energy loss dependence.

In Figure 14 the experimental data is plotted together with $(dE/dx)^2$ and $(dE/dx)^3$. In order to fit our data to these curves we had to shift the curves vertically by factors K respectively.

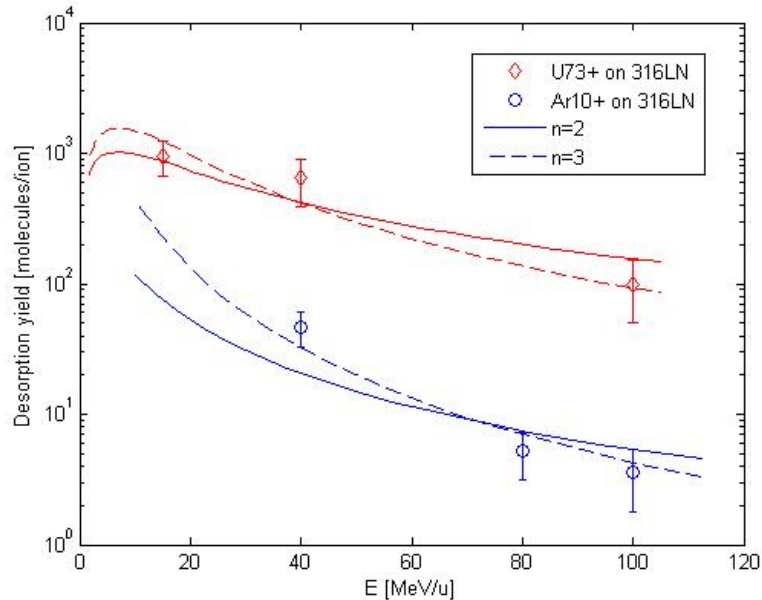


Figure 14: To fit our data to $(dE/dx)^2$ (solid lines) and $(dE/dx)^3$ (dashed lines), these curves had to be scaled by factors K respectively.

For the Ar^{10+} beam on 316LN stainless steel we roughly get $K = 1.9$ for $n=2$, and $K = 0.9$ for $n=3$. For the U^{73+} beam on 316 LN stainless steel we have the approximate value $K = 0.12$ for $n=2$, and $K=0.002$ for $n=3$, which differs a lot from the scaling of the Ar^{10+} beam. The difference in K factors is probably due to slightly changed experimental conditions.

5. Outlook

For the project with laser refractometry the next step is to build and perform measurements with the setup shown in Figure 6 and compare the obtained values with our theoretical values.

For the ion induced desorption project we are planning to build a new test stand at The Svedberg Laboratory, TSL, in Uppsala. There we will be able to perform measurements with argon beams at 15 MeV/u (to overlap with the GSI experiment) down towards 5 MeV/u. In the same run we will also perform measurements for other ions so that the scaling factors can be determined. It would also be interesting to study the angular dependence of the desorption yield.

6. Acknowledgements

First of all I would like to thank the AIM graduate school, the Swedish metrology institute, SP, and the Department of Nuclear and Particle Physics, IKP, for giving me the opportunity to work within the field of vacuum science.

To my supervisor Lars Westerberg; I am very grateful for your support and that you always, and I mean always, have time for my questions!

Leslie Pendrill, my co-supervisor: Even though you are far away you are easy to get hold of. You also have an ability to explain difficult things in an easy way. This I appreciate a lot.

Henrik: Thank you for making every day a bit brighter and for being the so needed “bollplank”.

I would not have been able to build the vacuum system at TSL without the great help from Carl-Johan Fridén, Peter Jahnke, Lars Pettersson, Lars-Olof Andersson and Trygve Johansen, whose knowledge is invaluable. Thank you all for your patience when I run after you in the corridors!

A special thanks goes to the vacuum group at GSI: Holger Kollmus, Markus Bender, Christina Bellachioma, Andreas Krämer and Hartmut Reich-Sprenger, together with Edgar Mahner at CERN and Oleg Malyshev at CCLRC Daresbury Laboratory, who kindly let me participate in their experiments. It has been very educational to take part in your discussions and you always made me feel very welcome.

Björgvin Hjörvarson: I am truly grateful for the fruitful discussions.

Jens Jensen: I really appreciate that you have taken the time with my project. Your engagement is encouraging!

Last, but not least, I thank the colleagues at TSL and IKP. A pleasant working environment is important to perform well.

7 References

- [1] C. Benvenuti and P. Chiggiato, "Obtention of pressures in the 10^{-14} torr range by means of a Zr---V---Fe non evaporable getter" *Vacuum*, **44**, 511-513 (1993)
- [2] P. Redhead, CERN Accelerator School on Vacuum Technology, CERN 99-05 (1999)
- [3] K. Jousten, H. Menzer, D. Wandrey and R. Niepraschk, "New, fully automated, primary standard for generating vacuum pressures between 10^{-10} Pa and 3×10^{-2} Pa with respect to residual pressure", *Metrologia*, **36**, 493-497 (1999)
- [4] J. F. O'Hanlon, "A User's Guide to Vacuum Technology", New Jersey : John Wiley & Sons Inc., , ch. 4, pp 57-76, 2003.
- [5] L. R. Pendrill, "Density of moist air monitored by laser refractometry", *Metrologia*, **25**, 87-93 (1988)
- [6] E. Hecht, "Optics" Addison Wesley, ISBN 0-201-30425-2, 1998
- [7] N. Khélifa, H. Fang, J. Xu, P. Juncar and M. Himbert, "Refractometer for tracking changes in the refractive index of air near 780 nm", *Appl. Opt.*, **37**, 156-161 (1998)
- [8] E. Mustafin et al., "A theory of the beam loss-induced vacuum instability applied to heavy-ion synchrotron SIS18", *Nucl. Inst. Meth. A*, **510**, 199-205 (2003)
- [9] <http://www-aix.gsi.de/accelerator/sis.p14.html>
- [10] <http://www-aix.gsi.de/accelerator/SD/ANGERT-INTASRGM020604.ppt>
- [11] H. Kollmus et al, AIP CP773, p. 207, 2005
- [12] P. Håkansson, "Desorption experiments on organic insulators with high energy particle beams", *Mat. Fys. Med.*, **43**, 593-622 (1993)
- [13] <http://www.srim.org>
- [14] K. Wien, "Fast heavy ion induced desorption", *Radiaton Effects and Defects in Solids*, **109**, 137-167, 1989
- [15] M. Beuve et al, "Influence of the spatial and temporal structure of the deposited-energy distribution in swift-ion-induced sputtering", *Phys. Rew. B*, **68**, 125423, 2003

Paper I

Improved determination of gas flow rate for UHV and leak metrology with laser refractometry

E. Hedlund¹ and L. R. Pendrill^{2,3}

¹Department of Nuclear and Particle Physics, Uppsala University, Box 535, SE-751 21 UPPSALA, Sweden

²SP Swedish National Testing & Research Institute, Measurement Technology, Box 857, SE-501 15 BORÅS, Sweden

³AIM Advanced Instrumentation and Measurements Graduate Programme, Box 535, SE-751 21 UPPSALA, Sweden

Abstract

A system often used for vacuum metrology purposes in order to calibrate vacuum gauges in the UHV region and to calibrate gas leak rates is the throughput system, employing the continuous (or dynamic) expansion method. An important component in such systems is the flowmeter, which has to deliver a pure and well-determined gasflow into the system. To determine the generated gas flow, a number of factors including the pressure inside the flowmeter have to be determined. However, it has turned out that the calibration uncertainty when measuring the pressure in the flowmeter gives a main contribution to the total uncertainty (of typically about 0.1%) for the generated flow, and thereby limiting the accuracies of the generated vacuum pressure as well as gas leak rates in UHV metrology. A feasibility study is reported in this paper about the possibility of using laser refractometry to monitor dynamic gas density *in situ* in the flowmeter, as an alternative and possibly more accurate means of determining the generated gas flow, thereby potentially improving the calibration gas leak rates in the range $10^{-8} - 10^{-4}$ Pa·m³/s.

1. Introduction

Many important industrial processes as well as fundamental scientific experiments are done in high vacuum and ultra-high vacuum (UHV), i.e. gas pressures down to 10^{-10} Pa [König *et al.* 2004]. These low pressures are essential in order to enable stable product processing conditions such as in the fast growing area of nanomaterials, where higher vacuum conditions are a prerequisite in meeting increased demands on limiting oxidation. Similarly, reliable measurement of UHV is essential in assessing factors (such as outgassing) limiting the high vacuum conditions necessary in physics experiments at large elementary particle accelerators. In these UHV applications, the vacuum gauges [Levin and Sweda 1997; Jousten *et al.* 1993; Jousten *et al.* 1999] and gas leaks [Jousten *et al.* 2002 and references therein] used have to be properly calibrated. The best means of determining pressures in this region to date employ the continuous expansion method, which has an uncertainty limited to typically 0.2% [Jousten *et al.* 1999]. Gas leaks can be determined with a similar set-up and with similar uncertainties.

1.1 The throughput system

A system often used for vacuum metrology, in order to generate accurate pressures in the vacuum region and to calibrate vacuum gauges (and leaks), is the throughput system based on the continuous expansion method. The throughput system consists of two vacuum chambers connected by an orifice, see Figure 1.

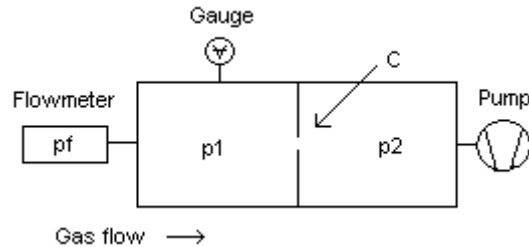


Figure 1: The throughput system. By knowing the gas flow generated from the flowmeter and the conductance of the small orifice, the pressure P_1 can be calculated.

The orifice, with approximately 1 cm diameter, sets a rather low conductance, and hence limits the possible pumping speed. Therefore the net pumping speed will be relatively independent of the speed of the pump.

The flowmeter, connected to the left as shown in figure 1, delivers a pure gas flow through a known conductance. By knowing the flow, q , from the flowmeter entering the vacuum chamber and also the outgoing flow through the orifice to the pumping chamber, one can get a good estimate of the pressure in the measuring chamber:

$$q = (P_1 - P_2) \cdot \frac{C}{A}, \quad (1)$$

where P_1 and P_2 are the pressures before and after the orifice, C is the conductance of the orifice and A is the area of the first vacuum chamber. Thus, by providing known flow rates of gas, known pressures can be generated [Levin and Sweda 1997]. An example of a particular design of flowmeter can be found at PTB in Berlin [Jousten *et al.* 1999] where the flowmeter consists of two volumes; a working volume and a reference volume. To achieve a constant flow leaving the flowmeter, the working volume is decreased continuously with a bellows. To determine the gas flow, q , the pressure in the flowmeter is typically determined with a capacitance diaphragm gauge (CDG) and a spinning rotor gauge (SRG). However, it has turned out that the main contributions to the total uncertainty of the generated flow of this flowmeter arise from the calibration error of the vacuum gauges measuring the pressure in the flowmeter [Jousten *et al.* 1993], see Figure 2.

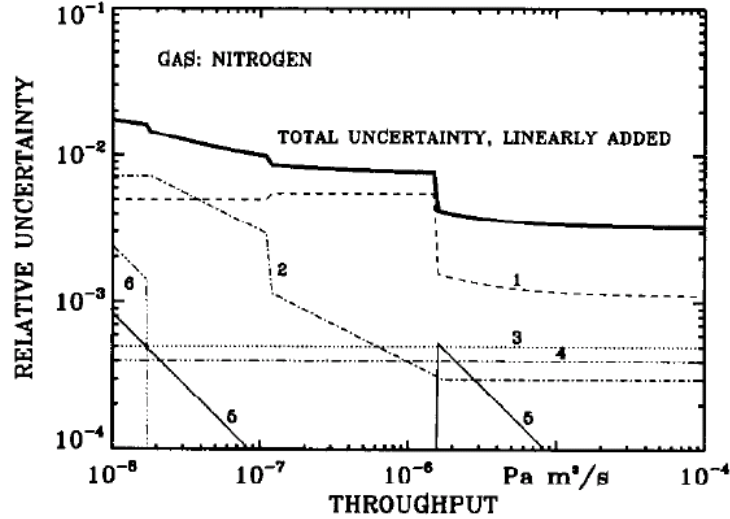


Figure 2: The total relative uncertainty of the flowmeter at PTB versus the throughput in $\text{Pa m}^3/\text{s}$ [K. Jousten *et al.* 1993]. 1) Calibration error of the instruments measuring pressure, 2) statistical uncertainty of time interval measurement, 3) systematic uncertainty of volume displacement, 4) systematic uncertainty of pressure measurement, 5) statistical uncertainty of pressure measurement, 6) systematic uncertainty of conductance.

In an alternative design at the Primary Standards Laboratory at Lockheed Martin Missiles and Space (LMMS), the pressure drop in the flowmeter is measured and compared to the corresponding pressure drop in the vacuum chamber [Levin and Sweda 1997]. Also here a CDG is used to measure the pressure in the flowmeter in order to determine the gas flow and thereby the generated vacuum pressure.

Since the accuracy of these vacuum gauges is the main limiting factor to the total accuracy of the flowmeter, another way of measuring the gas flow rate has to be found if accuracies in UHV metrology and leak rate metrology are to be achieved. In this article focus has been on the possibility to use laser refractometry in order to measure the gas density and thereby obtaining the gas flow rate from the flowmeter. This novel method is one of a class of optical methods recently developed with application to gas pressure measurement [Lanzinger *et al.* 1998, Pendrill 2004]

2. Derivation of gas flow as a function of gas density

The basis of the proposed method of determining gas flow more accurately with the continuous expansion method is to replace measurement of the pressure in the flowmeter, as in case of traditional throughput systems [§1.1], with a measurement of the gas density, ρ .

The flow, q , generated by the flowmeter can be expressed in terms of the pressure and rate of change in volume of the flowmeter [Jousten *et al.* 1999, equation (8)]:

$$q = p \cdot \frac{\Delta V}{\Delta t} \quad (2)$$

The equation-of-state of an ideal¹ gas:

$$p = \rho RT = \frac{n}{V} \cdot RT \quad (3)$$

where T is the temperature, R is the molar gas constant and n is the number of gas molecules in a volume V , referred to a molar volume, hence ρ is expressed in units of mol m^{-3} .

Combining (2) and (3) yields the expression:

$$q = RT \cdot \frac{\Delta\rho}{\Delta t} \quad (4)$$

Thus a measurement of the rate of change of gas density will yield an alternative estimate of gas flowrate than the traditional expression (2).

New methods of measuring gas density, particularly those based on refractometry [Pendriill 1988, 2004], which have been developed recently, can with advantage be applied to gas flow determination according to equation (4).

3. Refractometry

Refractometry is a technique that measures how light is refracted when it passes through a given substance, that is, how the speed of light is changed by density of the substance. The obtained refractive index is then directly proportional to the gas density when studying a gaseous medium, thereby providing a method that is non-intrusive and dynamic [Pendriill 1988, 2004]. It is a closely related, but alternative method to optical spectroscopy using absorption instead [Lanzinger *et al.* 1998] in the determination of gas pressures and densities.

In a comparison of different methods to monitor air density, it has been found earlier that the values from the measurements made with laser refractometry were very close to the alternative estimates of air density, obtained with other methods such as the equation-of-state [Davis 1992] and the weighing of air buoyancy artefacts. The resolution of the laser refractometry measurements of gas density was on the order of parts in 10^5 [Pendriill 1988]. We are therefore interested to investigate whether laser refractometry can be employed to obtain high accuracy measurements of the gas flow, through dynamic gas density determination which might ultimately lead to improved determination of UHV pressures and gas leak rates using the continuous (or dynamic) expansion method.

¹ Gas non-ideality can be expressed in terms of a compressibility factor Z or virial coefficients B and C , which are small but known factors for air [Davis 1992]

3.1 Interferometers

In order to measure a change in refractive index of a gas, an optical interferometer is often used. Two common types of refractometer are the Michelson interferometer and the Fabry-Perot interferometer. Because of the high resolution, simplicity and compactness of the setup, the Fabry-Perot interferometer has been chosen for this feasibility study. More detailed descriptions of these interferometers may be found in standard monographs in optics, for example [Hecht, 1998]

4. Derivation of gas density as a function of refractive index

The Lorentz-Lorenz formula relates the refractive index, n , of a gas to its density, ρ , as:

$$\frac{n^2 - 1}{n^2 + 2} \approx \frac{2}{3}(n - 1) = \frac{P}{RT} \cdot \sum_i x_i A_i = \rho \cdot \sum_i x_i A_i \quad (5)$$

where A_i is the molecular polarizability of a gas component of relative concentration x_i . The value of A_i for respective gases can be found in [Peck and Khanna 1966].

Rearranging (5) gives:

$$\rho = \frac{\sum_i x_i}{\sum_i x_i A_i} \cdot \frac{2}{3}(n - 1) \quad (6)$$

Since we are interested in the mass density change we perform a derivation of (6) with respect to n :

$$\Delta\rho = \frac{\sum_i x_i}{\sum_i x_i A_i} \cdot \frac{2}{3} \Delta n \quad (7)$$

To get a value of Δn , we consider the resonance condition for a Fabry-Perot refractometer:

$$\frac{m\lambda}{2} = nd \quad (8)$$

Combining $c=v\lambda$ with (8) we get:

$$v = \frac{mc}{2nd} \quad (9)$$

Performing a derivation of (9) with respect to n gives:

$$\Delta\nu = \frac{mc}{2d} \cdot \frac{\Delta n}{n^2} \quad (10)$$

Substituting m from (9) and putting it in (10) gives:

$$\Delta\nu = \nu \cdot \frac{\Delta n}{n} \quad (11)$$

By combining (7) and (11) we see that a change in frequency (the only parameter we can measure) will lead to a change in the refractive index and hence a change in the mass density:

$$\Delta\rho = \frac{\sum_i x_i}{\sum_i x_i A_i} \cdot \frac{2n}{3\nu} \cdot \Delta\nu \quad (12)$$

where n can be obtained from equation (10), ν is the frequency of the laser and $\Delta\nu$ is the relative frequency change measured by the Fabry-Perot interferometer. Inserting (12) in (4) gives:

$$q = RT \cdot \frac{\sum_i x_i}{\sum_i x_i A_i} \cdot \frac{2n}{3\nu} \cdot \frac{\Delta\nu}{\Delta t} \quad (13)$$

5. Results and discussion

Our planned setup is shown in figure 3 [Khélifa *et al.* 1998]. We will use a laser with a wavelength of 1064 nm controlled by a current driver. The laser beam passes through an isolator before entering the Fabry-Perot cell and finally is detected in a fast photo diode (bandwidth > 1 GHz). By reconnecting the current to the current driver via an amplifier, one can adjust the laser to the wanted peaks. Using heterodyne spectroscopy there will be enough accuracy to determine a frequency difference of 10 kHz.

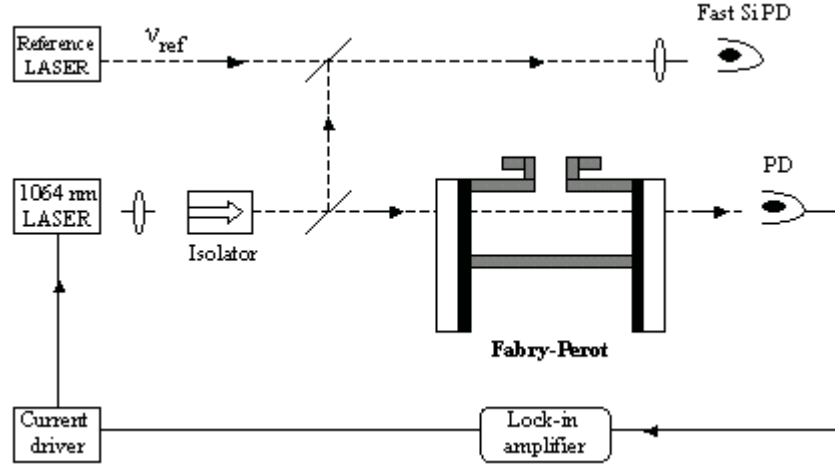


Figure 3: The planned setup is based on heterodyne spectroscopy in order to obtain enough accuracy to determine a frequency difference of 10 kHz.

We have found mirrors commercially available with a reflectivity of $R = 99.999\%$ for a wavelength of 1064 nm. Using this reflectivity we obtain a finesse of $3.14 \cdot 10^5$. If we then set the distance between the mirrors to $d = 1$ mm we obtain the value of $\Delta\nu/2$ of the spectral halfwidth of the Fabry-Perot transmission peaks to be $2.39 \cdot 10^5$ Hz.

The refractive index of a gas varies with temperature. But, a temperature change may also affect the ‘mechanical’ length of the refractometer and it will be necessary to separate these two temperature effects. For example, a temperature change of 6 mK for a period of 6 hours could lead to a length change of over 3 nm [Pendrell 2004]. In our setup the distance between the mirrors are comparably small and to get a length change of 3 nm the temperature will have to change by 3 K. Still, care must be taken to compensate for temperature differences. We estimate the temperature accuracy to 0.2 %. Due to these temperature effects it is important to perform a calibration of the distance between the mirrors before the measurement.

The laser is estimated to be within 10 % of $\Delta\nu$. This gives:

$$\Delta\nu_{finesse} = \frac{1}{10} \cdot \frac{\Delta\nu}{2} = \frac{FSR(1-R)}{10 \cdot 2 \cdot \pi \cdot \sqrt{R}} \quad (15)$$

For a distance between the mirrors of $d = 1$ mm we get the free spectral range $FSR = 1.5 \cdot 10^{11}$ Hz. Using this value and the reflectivity $R = 99.999\%$ we get $\Delta\nu_{finesse} = 2.39 \cdot 10^4$ Hz.

Using $n^2 \approx 1$, $M_{N_2} = 28.0134 \cdot 10^{-3}$ kg/mole and $A_{N_2} = 4.4464 \cdot 10^{-6}$ m³/mole for nitrogen [Peck and Khanna 1966] we have:

$$\Delta\rho_{finesse} = \frac{2}{3} \cdot \frac{M_{N_2}}{A_{N_2}} \cdot \frac{2d}{mc} \cdot \Delta\nu_{finesse} = 1.79 \cdot 10^{-5} \text{ kg/m}^3 \quad (16)$$

Assuming that the pressure in the flowmeter, p_f , is 10^3 Pa we get that $\rho = 0.4295$ mol/m³.

The relative resolution in gas density is then:

$$\frac{\Delta\rho_{\text{finesse}}}{\rho} = 4.17 \cdot 10^{-5} \quad (17)$$

The resolution in gas density is pressure dependent: if the pressure decreases with a factor 10 the resolution will worsen by a factor 10. The resolution is also affected by the distance between the mirrors: by increasing d with a factor two, the resolution will improve by a factor two. In figure 7 below the relative resolution of the gas density for nitrogen is plotted as a function of the flow generated by the flowmeter. In the same plot, a very rough plot of the inaccuracy of the fill pressure measurement for nitrogen taken from the article by [Jousten *et al.* 1999], are shown as a comparison.

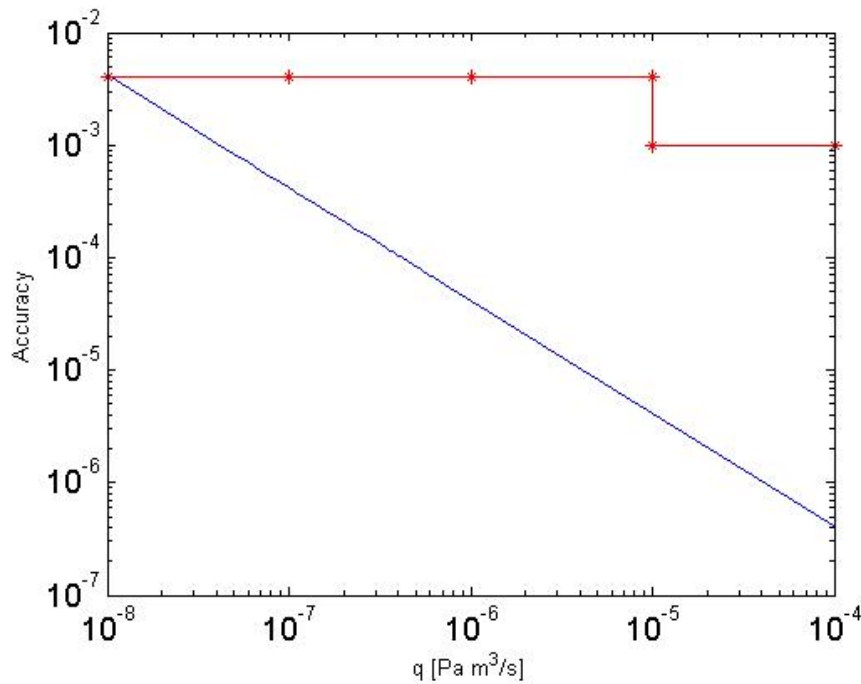


Figure 4: A plot of the inaccuracy as a function of the generated flow from the flowmeter. The solid line is the theoretical values of the resolution obtained by the laser refractometry method, and the line with stars is the inaccuracy coming from the fill pressure measurements by [Jousten *et al.* 1999].

The uncertainty for the fill pressure measurement in the flowmeter at PTB was about $1 \cdot 10^{-3}$ for a gas flow of $1 \cdot 10^{-4}$ Pa m³/s. For the laser refractometry method the resolution is around $4 \cdot 10^{-7}$ for the same pressure. Hence, the accuracy is roughly 3 orders of magnitude lower in the later case. But, as the pressure decreases, the accuracy will increase linearly for the laser refractometry method, and at a gas flow of $1 \cdot 10^{-8}$ Pa m³/s the accuracy of the both methods are the same. It is important to remember that our values are theoretical values, and the values from [Jousten *et al.* 1999] are experimental data. However, the laser refractometry method is a promising new method in order to determine the gas flow. The next step is to perform

measurements with the setup shown in figure 3 and compare the obtained values with our theoretical values.

6. Acknowledgement

The authors would like to thank the AIM graduate school and SP for supporting this project. We are also very grateful to Karl Jousten and his group at PTB Berlin (DE) for fruitful discussions. We appreciate useful references sent to us from Charles D Ehrlich of NIST (USA)

7. References

Davis R S, "Equation for the determination of the density of moist air", *Metrologia*, **29**, 67-70 (1992)

Hecht E, "Optics" Addison Wesley, ISBN 0-201-30425-2, 1998

Jousten K, Messer G and Wandrey D, "A precision gas flowmeter for vacuum metrology", *Vacuum*, **44**, 135-141 (1993)

Jousten K, Menzer H, Wandrey D and Niepraschk R, "New, fully automated, primary standard for generating vacuum pressures between 10^{-10} Pa and 3×10^{-2} Pa with respect to residual pressure", *Metrologia*, **36**, 493-497 (1999)

Jousten K, Menzer H and Niepraschk R, "New, fully automated, gas flowmeter at the PTB for flow rates between 10^{-13} mol/s and 10^{-6} mol/s", *Metrologia*, **39**, 519 - 529 (2002)

Khélifa N, Fang H, Xu J, Juncar P and Himbert M, "Refractometer for tracking changes in the refractive index of air near 780 nm", *Appl. Opt.*, **37**, 156-161 (1998)

König V, Ackerholm M and Arrhén F, "The need of traceable measurements of vacuum in industry and research in the Nordic countries", *International Vacuum Conference IVC-16*, Venice (IT) June-July (2004).

Lanzinger E, Jousten K and Kühne M, "Partial pressure measurement by means of infrared laser absorption spectroscopy", *Vacuum*, **51**, 47 – 51 (1998)

Levin P D and Sweda J R, "Precision gas flowmeter for vacuum calibration", *J. Vac. Sci. Technol. A*, **15(3)**, 747-752 (1997)

Peck E R and Khanna B N, "Dispersion of argon", *J. Opt. Soc. Am.*, **56**, 1059-1063 (1966)

Pendrill L R, "Density of moist air monitored by laser refractometry", *Metrologia*, **25**, 87-93 (1988)

Pendrill L R, "Refractometry and gas density", *Metrologia*, **41**, S40-S51 (2004)

Paper II

Energy dependence of normal incidence ion-induced desorption yields measured with U^{73+} and Ar^{10+} ions in the 15-1000 MeV/u energy region

E. Hedlund¹, M. Bender², M.C. Bellachioma², E. Mahner³, A. Kraemer²,
L. Westerberg⁴, O.B. Malyshev⁵, H. Reich-Sprenger², and H. Kollmus²

¹*Department of Nuclear and Particle Physics, Uppsala University, Uppsala, Sweden*

²*Gesellschaft für Schwerionenforschung, Darmstadt, Germany*

³*CERN, Geneva, Switzerland*

⁴*The Svedberg Laboratory, Uppsala University, Uppsala, Sweden*

⁵*CCLRC Daresbury Laboratory, Warrington, UK*

Abstract

Large pressure rises, up to a several orders of magnitude, due to ion-beam loss induced desorption have been observed during operation of heavy ion accelerators at CERN, GSI and BNL. In previous measurements at GSI with 1.4 MeV/u beams, a $(dE/dx)^2$ scaling of the desorption yield η (released molecules per incident ion) was found for different incident ions. In order to verify this scaling we first made experiments with U^{73+} beam impacting on 316LN and P506 stainless steel, OFE copper and aluminum targets for the energies 15, 40, 100, 408 and 1000 MeV/u. In a second experiment we used Ar^{10+} beam impacting on 316LN stainless steel for 40, 80 and 100 MeV/u. The measured effective desorption yields were compared with theoretical values of the electronic energy loss, dE/dx .

Introduction

The heavy ion accelerators at CERN, GSI and BNL have shown large pressure rises during operation [1]. The instability of the vacuum is a problem since it will limit the intensity and lifetime of the beam. When lost beam ions hit the vacuum chamber wall large amounts of gas molecules are released, which cause the large pressure rises. During recent years experiments have been performed to study desorption yields η [2-5]. The desorption yield (released molecules per incoming ion) has been found to be of the order of up to 10^5 molecules/ion. Hence, to cure the vacuum instabilities a better understanding of theoretical aspects of the heavy ion beam induced desorption is important. In this study the focus has been on how the desorption yield is related to the choice of material, impacting energies and ions. In previous measurements at GSI for beams of 1.4 MeV/u, a $(dE/dx)^2$ scaling was found for the different incident ions [6]. In order to verify this scaling two different incident ions, U^{73+} and Ar^{10+} , with energies ranging from 15 to 1000 MeV/u have been used in the experiments presented in this paper.

Theory

When a solid target is hit by a heavy ion, atoms or molecules are released from the surface. The desorption mechanism could be explained by the energy loss of the projectile ion in form of nuclear and electronic stopping [7]:

$$\frac{dE}{dx} = \left(\frac{dE}{dx} \right)_n + \left(\frac{dE}{dx} \right)_e \quad (1)$$

Whether the energy loss is mainly due to nuclear or electronic stopping depends of the velocity of the heavy ion [8]. If the velocity is below the Bohr velocity (0.22 cm/ns), the electrons in the target are moving much faster than the projectile ion. There will mainly be an elastic collision, and then the energy loss is due to nuclear scattering. The projectile nucleus can also interact inelastically with a target atom, but the main interaction will be elastic scattering. Above the Bohr velocity the energy loss is dominated by electronic stopping. Due to the high velocity of the projectile ion the collision between the incoming ion and the target electrons will be inelastic. The transformed kinetic energy will either excite an electron or ionize the atom. In our experiment the velocity of the heavy ions are well above the Bohr velocity, and hence the energy loss is mainly due to electronic stopping. In the electronic stopping region there are several theories on how the energy is deposited and on what mechanisms that will lead to desorption. The three main models describing the process of sputtering yield are the Coulomb explosion model, the thermal spike model and the pressure-pulse model [9, 10]. The models predict different values of the exponent n on the energy loss dependence of the desorption yield as $\text{Yield} \propto (dE/dx)^n$, where n ranges from 1.5-3.

Coulomb explosion model

When the projectile ion hits the target it could lead to extremely high deposited energy densities [9, 11]. This could lead to ejection of δ -electrons, leaving a positive ion core formed along the ion track. Due to Coulomb repulsion, the ion core will explode and in turn generate a low energy atomic collision cascade. There are different theories on what will happen after the collision cascade. One theory is that the explosion heats up the solid and therefore desorption is due to thermal evaporation. In another theory it is assumed that the cascade of particles resulting from the collision will form a radially moving shockwave, and when the wave is impacting on the surface materials will be released [12, 13]. Coulomb explosion is very likely in insulators, where electrons are rare. The coulomb explosion model predicts an energy loss scaling of the yield as $\text{Yield} \propto (dE/dx)^{1.5}$.

Thermal spike model

The energy is first deposited locally, within a small volume, on the electrons of the target [9, 11, 14]. Thereafter the electron-phonon coupling transfers the energy to the atomic subsystem. How the energy is spread in the electron subsystem depends on the electron mobility. The spike in this model is an area with a high energy density along the ion track. In the spike volume almost all atoms are in motion due to the high density of the of the recoil cascade [11]. Since the spike is very hot, a plasma is created in the core,

which in turn will lead to desorption by an evaporation process. Desorption could also be a result of a sublimation process from the heated areas around the core. The thermal spike model predicts $\text{Yield} \propto (dE/dx)^2$.

Pressure-pulse model

In this model the projectile ion will excite the target atoms, which causes them to expand and hence there will be a pressure onto the boundaries of a lattice cell [9, 14]. There are several different types of pressure-pulse models. One model is based on the assumption that when a molecule at the surface is expanding, it will repel itself from its neighbours and desorb into the vacuum. The pressure-pulse model is mostly used to describe processes where large molecules are sputtered from the surface. This model predicts $\text{Yield} \propto (dE/dx)^3$.

Experiment

Uranium beam

An overview of the setup for the U^{73+} beam experiment is shown in figure 1 [6]. In order to reduce the pressure from 10^{-7} mbar in the beam line to the required 10^{-11} mbar there are three differential pumping stages in front of the experimental chamber. The different samples are 316LN stainless steel, P506 stainless steel, OFE copper and 6082 aluminum, all mounted on a linear and rotational feedthrough.

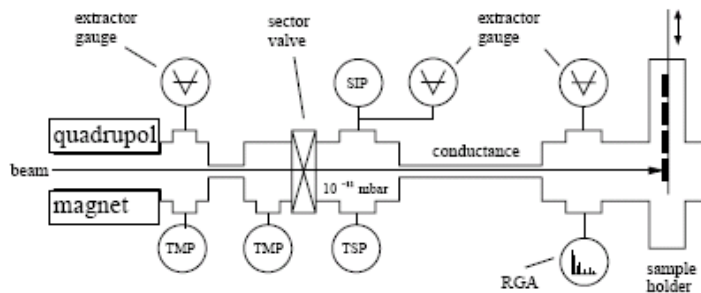


Figure 1: The experimental setup.

The thickness of each sample was chosen in order to be larger than the penetration depth of the projectile ions. For each measurement a new unused sample was selected to avoid uncertainties due to cleaning effects. During the ion bombardment, all performed at perpendicular incidence, the total pressure increase was measured with an extractor ionization gauge while the partial pressure distribution was registered by a residual gas analyzer (RGA). The projectile energies were chosen to 15, 40, 100, 408 and 1000 MeV/u. The size of the ion beam on the targets can be adjusted using the quadrupole magnets in the beam line. To see if the ion beam would hit the targets an Al_2O_3 fluorescence screen was mounted on the target holder. The projectile ion current is measured using current transformers in the SIS18 and in the beam line to the experiment.

The effective desorption yield η_{eff} was calculated from the total pressure increase Δp using the ideal gas law,

$$\eta_{\text{eff}} = \frac{\Delta p \cdot S}{\dot{N} \cdot k_B \cdot T} \quad (2)$$

where S is the pumping speed, \dot{N} is the projectile ion flux, k_B the Boltzmann constant and T the temperature. “Effective” desorption means that all values might have the same systematic error, e.g. from the pressure measurement or from the pumping speed used in formula (1), which depends on the partial pressure distribution.

The SIS18 accelerator at GSI was providing a mean number of $2.4 \cdot 10^8$ U^{73+} particles per hit every 3.9 s, giving an average flux of $7.2 \cdot 10^7$ particles/s. The corresponding pressure increase Δp was about $1 \cdot 10^{-10}$ mbar. The base pressure was in the 10^{-9} mbar range. In figure 2 a typical pressure evolution under ion bombardment recorded with the extractor ionization gauge calibrated for N_2 is shown.

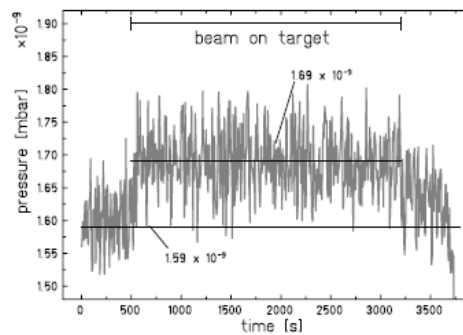


Figure 2: A typical pressure evolution under ion bombardment recorded with the extractor ionization gauge calibrated for N_2

Partial ion currents for H_2 , CH_4 , CO and CO_2 were recorded simultaneously by the RGA. Only a partial pressure increase for CO and CH_4 was detected on an H_2 dominated background.

Argon beam

Before the measurements with the Ar^{10+} beam were started the experimental setup was modified in order to achieve a lower base pressure. Since the target holder itself turned out to be a source of high outgassing when it was moving to the respective sample, the target holder was removed and the sample was instead simply the end flange made of 316LN stainless steel. To improve the pumping speed of the system, the aperture of the pumping stages was increased and partially thin film NEG coated. For alignment and diagnosis of the beam a current transformer and an Al_2O_3 fluorescence beam screen were added. The beam current had a flux between $9 \cdot 10^9$ and $7.5 \cdot 10^{10}$ particles/sec, resulting in a pressure increase of between $2.7 \cdot 10^{-11}$ and $1.8 \cdot 10^{-10}$ [15]. The projectile energies were chosen to 40, 80 and 100 MeV/u. The RGA was broken in the beginning of the experiment, therefore no information about the partial pressure could be obtained.

Results and Discussion

The effective desorption yields for the U^{73+} and Ar^{10+} beams on different target and energies are summarized in table 1.

Table 1: Experimental data

| Run | Energy [MeV/u] | η |
|---------------------|-----------------------|--------------------------|
| Ar^{10+} on 316LN | 40 | 47 (40%) |
| | 80 | 5.2 (60%) |
| | 100 | 3.6 (60%) |
| $U73^+$ on 316LN | 15 | 950 (30%) |
| | 40 | 650 (40%) |
| | 100 | 100 (50%) |
| $U73^+$ on Al | 15 | 1200 (30%) |
| | 40 | 680 (40%) |
| | 100 | 200 (50%) |
| $U73^+$ on Cu | 15 | 550 (30%) |
| | 40 | 410 (40%) |
| | 100 | 120 (50%) |
| $U73^+$ on P506 | 15 | 820 (30%) |
| | 40 | 770 (40%) |
| | 100 | 255 (50%) |

The effective desorption yields for the U^{73+} and Ar^{10+} beams on 316LN stainless steel are plotted in figure 3. There are no data points available for the U^{73+} beam at 408 and 1000 MeV/u since the detection limit was too low. For a base pressure in the low 10^{-10} mbar region, an upper limit for the effective desorption yields for these two energies was around 200 particles per incident ion for all targets.

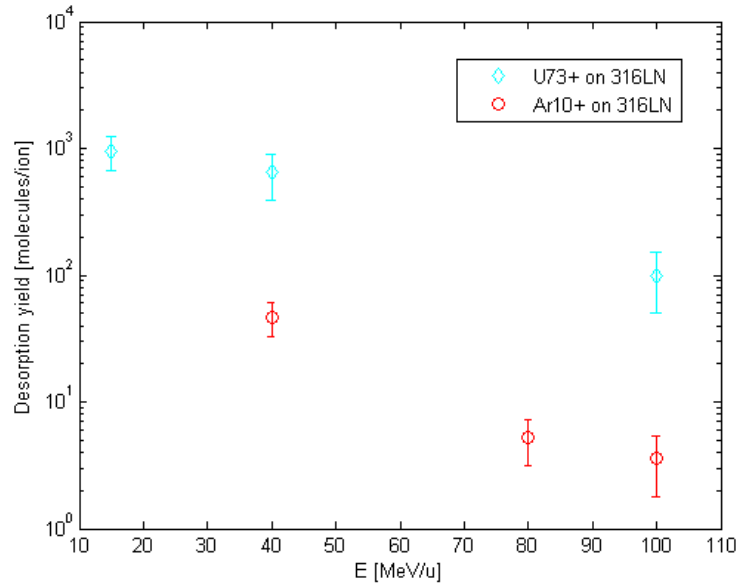


Figure 3: The obtained desorption yields from U^{73+} and Ar^{10+} beams impacting on 316LN stainless steel in the 15-100 MeV/u energy range

One can clearly see that the effective desorption yield is decreasing with increasing projectile energy. For the uranium beam we observe different desorption yields for the four different targets, see figure 4. The general trend is that the yield from the copper target is lower than that of the other targets.

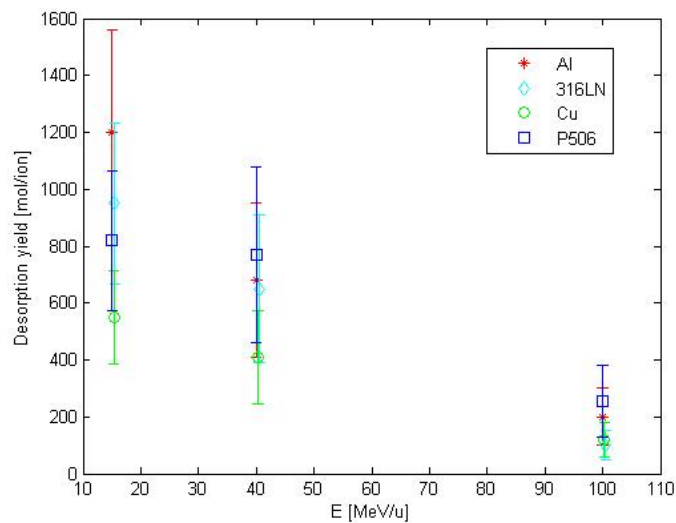


Figure 4: Desorption yields from uranium beam impacting on different targets.

If we compare the desorption coefficients obtained for uranium and argon impacting on the stainless steel target, huge differences in desorption yields are observed. We assume that the desorption is due to processes in a critical region from the surface down to a

certain depth shorter than the range of these high-energy particles. In the critical region for these high energies dE/dx will be approximately constant for the respective ions. Ideally one would like to compare the deposited energy per unit volume for uranium and argon. According to the SRIM code, dE/dx for uranium is much higher than for argon for the same critical length in the sample, which could in part explain the higher desorption yields for uranium.

Here, we can investigate how the effective desorption yield scales with the energy loss, i.e. we would like to find the values for the scaling factor K and the exponent n from the following equation

$$\eta_{eff} = K \cdot \left(\frac{dE}{dx} \right)^n \quad (3)$$

By expressing the effective desorption yield in terms of the corresponding energy loss, we obtain a value of the exponent n from the slope of the lines, see figure 5. For the U^{73+} beam $n = 2.6 \pm 0.5$ and for the Ar^{10+} beam $n = 3.6 \pm 2.5$.

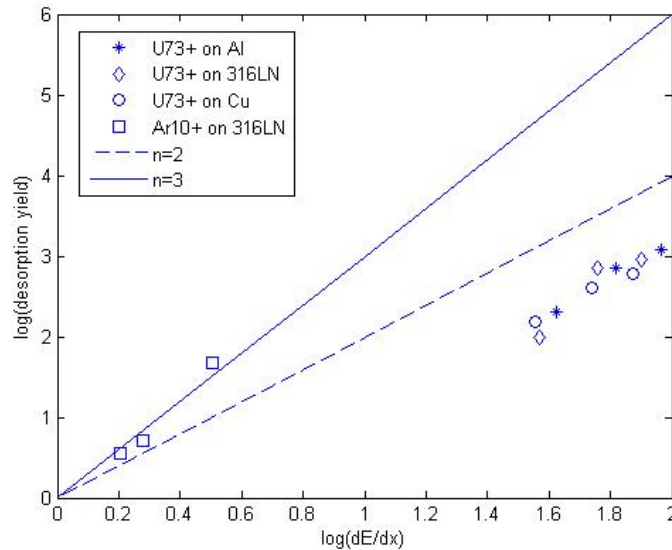


Figure 5: Effective desorption yields from aluminium, copper and stainless steel as a function of the energy loss. For Ar on 316LN $n = 3.6$. For the U beam on Cu we get $n = 1.9$, on 316LN $n = 2.9$ and on Al $n = 2.3$.

In figure 6 the solid line represents $(dE/dx)^2$ and the dashed line $(dE/dx)^3$ as functions of the projectile energies. In order to fit our data to these curves we had to shift the curves vertically by factors K respectively.

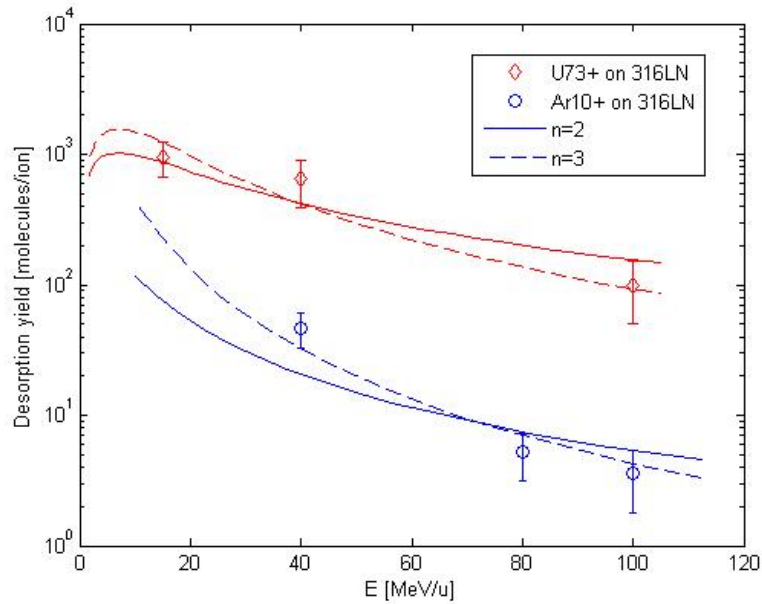


Figure 6: To fit our data to $(dE/dx)^2$ (solid lines) and $(dE/dx)^3$ (dashed lines), these curves had to be scaled by factors K respectively.

For the Ar^{10+} beam on 316LN stainless steel we roughly get $K = 1.9$ for $n=2$, and $K = 0.9$ for $n=3$. For the U^{73+} beam on 316 LN stainless steel we have the approximate value $K = 0.12$ for $n=2$, and $K=0.002$ for $n=3$, which differs a lot from the scaling of the Ar^{10+} beam. We believe this is probably due to slightly changed experimental conditions which may affect the residual gas composition, but it could also be an effect of different effective desorption due to different interaction volumes for the uranium and argon ions.

Another factor that could affect the yield could be the different charge states of the projectile. For lower energies (< 1 MeV/u) this is the case due to e.g. surface effects [16]. For higher projectile energies the equilibrium charge state distribution will be reached at a certain depth. From our data we cannot draw any conclusion whether this depth is within the critical volume for desorption.

Conclusions

The effective desorption yields versus beam energy can be described as a scaling factor K and an exponential dependence of the energy loss as in eq. (3). We deduce exponents to be between 2 and 3, which is slightly higher than predicted by the thermal spike model. The general trend of the desorption yields from the uranium experiment is that the desorption yield from the copper target is lower than that of the other targets.

References

- [1] E. Mustafin et al., "A theory of the beam loss-induced vacuum instability applied to heavy-ion synchrotron SIS18", *Nucl. Inst. Meth. A* **510**, 199-205 (2003)
- [2] J. Bossler et al., "Experimental investigation of electron cooling and staking of lead ions in a low energy accumulator ring", *Laboratory Note CERN-PS-99-033-DI* (1999)
- [3] E. Mahner et al., "Beam-loss induced pressure rise of Large Hadron Collider collimator materials irradiated with 158 GeV/u In⁴⁹⁺ ions at the CERN Super Proton Synchrotron", *Physical Review Special Topics-Accelerators and Beams* **7**, 103202 (2004)
- [4] E. Mahner et al., "Ion-stimulated gas desorption yields of electropolished, chemically etched, and coated (Au, Ag, Pd, TiZrV) stainless steel vacuum chambers and St707 getter strips irradiated with 4.2 MeV/u lead ions", *Physical Review Special Topics Accelerators and Beams* **8**, 053201 (2005)
- [5] E. Mahner et al., "Molecular desorption of stainless steel vacuum chambers irradiated with 4.2 MeV/u lead ions", *Physical Review Special Topics-Accelerators and Beams* **6**, 013201 (2003)
- [6] H. Kollmus et al, AIP CP773, p. 207 (2005)
- [7] G. Betz and K. Wien, "Energy and angular distributions of sputtered particles", *Int. J. of Mass Spectrometry and Ion Processes* **140**, 1-110 (1994)
- [8] A. W. Molvik et al, "Gas desorption and electron emission from 1 MeV potassium ion bombardment of stainless steel", *Physical Review Special Topics-Accelerators and Beams* **7**, 093202 (2004)
- [9] K. Wien, "Fast heavy ion induced desorption", *Radiation Effects and Defects in Solids* **109**, 137-167 (1989)
- [10] M. Beuve et al, "Influence of the spatial and temporal structure of the deposited-energy distribution in swift-ion-induced sputtering", *Phys. Rev.* **B68**, 125423 (2003)
- [11] C. T. Reimann, "Theoretical models for sputtering and desorption of bio-organic molecules under collisional and electronic excitation by ion impact", *Mat. Fys. Med.* **43**, 351-401 (1993)
- [12] Y. Hayaschiuchi et al., *J. Nucl. Materials* **71**, 181-186 (1977)
- [13] I. S. Bitensky and E. S. Parilis, *Nucl. Inst. Meth.* **B21**, 26-36 (1987)
- [14] H.D. Mieskes et al, "Electronic and nuclear thermal spike effects in sputtering of metals with energetic heavy ions", *Phys. Rev.* **B67**, 155414 (2003)
- [15] M. Bender et al, GSI Annual Report, (2005) (to be published)
- [16] P. Håkansson, "Desorption experiments on organic insulators with high energy particle beams", *Mat. Fys. Med.* **43**, 593-622 (1993)